Single-Layer Metasurface with Controllable Multiwavelength Functions

Zhujun Shi,[†,○] Mohammadreza Khorasaninejad,[‡,○] Yao-Wei Huang,[‡,§,○] Charles Roques-Carmes,[‡] Alexander Y. Zhu,[‡] Wei Ting Chen,[‡] Vyshakh Sanjeev,[‡,∥] Zhao-Wei Ding,[‡,∥] Michele Tamagnone,[‡] Kundan Chaudhary,[‡] Robert C. Devlin,[‡] Cheng-Wei Qiu,[§,⊥,#] and Federico Capasso*,[‡]

[†]Harvard Department of Physics, Harvard University, Cambridge, Massachusetts 02138, United States

[‡]Harvard John A. Paulson School of Engineering and Applied Sciences, Harvard University, Cambridge, Massachusetts 02138, United States

[§]Department of Electrical and Computer Engineering, National University of Singapore, Singapore 117583, Singapore

[∥]University of Waterloo, Waterloo, ON N2L 3G1, Canada

[⊥]NUS Suzhou Research Institute (NUSRI), Suzhou Industrial Park, Suzhou 215123, China

[#]SZU-NUS Collaborative Innovation Center for Optoelectronic Science & Technology, Shenzhen University, Shenzhen 518060, China

S Supporting Information

ABSTRACT: In this paper, we report dispersion-engineered metasurfaces with distinct functionalities controlled by wavelength. Unlike previous approaches based on spatial multiplexing or vertical stacking of metasurfaces, we utilize a single phase profile with wavelength dependence encoded in the phase shifters' dispersion. We designed and fabricated a multiwavelength achromatic metalens (MAM) with achromatic focusing for blue (B), green (G), yellow (Y), and red (R) light and two wavelength-controlled beam generators (WCBG): one focuses light with orbital angular momentum (OAM) states ($l = 0,1,2$) corresponding to three primary colors; the other produces ordinary focal spots ($l = 0$) for red and green light, while generating a vortex beam ($l = 1$) in the blue. A full color (RGB) hologram is also demonstrated in simulation. Our approach opens a path to applications ranging from near-eye displays and holography to compact multiwavelength beam generation.
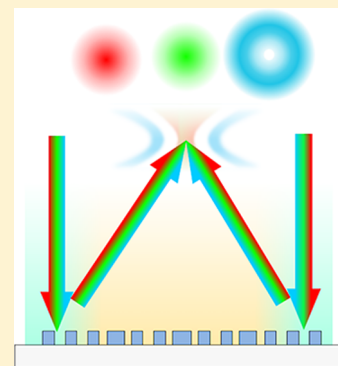
KEYWORDS: Metasurface, dispersion engineering, visible spectrum, titanium dioxide, orbital angular momentum states, achromatic metalens

Metasurfaces are ultrathin planar optical components consisting of subwavelength spaced scatterers patterned at an interface. Arrays of scatterers with proper geometrical parameters and orientation can control, often simultaneously, phase, amplitude, and polarization of the scattered wave-front.[1−4] The introduction and development of metasurfaces have led to new physics such as the generalized laws of reflection and refraction,[5] generalized Brewster effect,[6] as well as numerous technologically important devices/systems such as flat lenses (metalenses),[7−10] holograms,[11−13] structured beam generators,[14−19] ultracompact spectrometers,[20,21] polarime-ters,[22−24] etc. Compared with conventional refractive optics, metasurface-based optical elements have the advantages of lightweight, compactness, and the ease to control the phase profile, offering great potential in the integration and miniaturization of current bulky optical devices.

A major advantage of metasurfaces is their multifunctionality. It has been shown that a single metasurface can combine distinct functionalities without significant addition of design and fabrication complexity.[25−28] For example, metasurfaces can

implement distinct tasks depending on the input polar-ization.[29−33] By combining the geometric and propagation phase, it has been shown that the phases for two orthogonal polarizations can be completely decoupled.[34] It is highly desirable if similar capability can be achieved in the spectral domain. That is, one can design metasurfaces to have completely different functionalities controlled by wavelength (wavelength-controlled metasurfaces). The latter requires the ability to independently implement arbitrary phase profiles at different wavelengths. This is, in general, not achievable with either refractive optics or conventional diffractive optics, where the spectral response is dominated by material dispersion and dispersion from grating effects, respectively. In both cases, there is no degree of freedom to tune the phases at different

wavelengths separately, and the device function at one wavelength is predetermined by that at another wavelength.

One direct application of wavelength-controlled metasurfaces is a multiwavelength achromatic metalens (MAM) [Figure 1a].
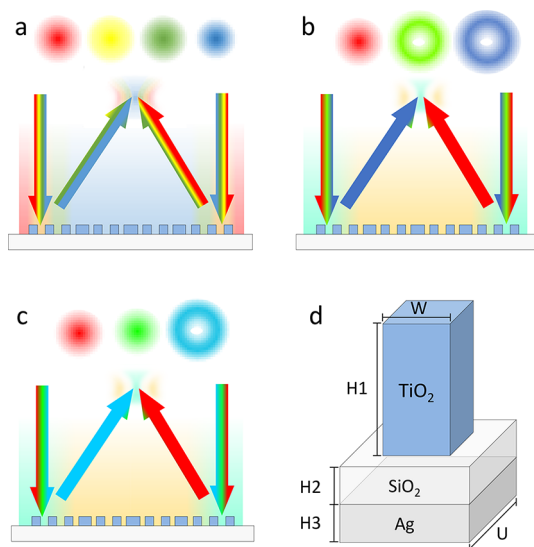

Figure 1. (a) Schematic view of multiwavelength achromatic metalens (MAM). Four different wavelengths (R, Y, G, and B) are focused at the same distance. (b) Schematic view of the first wavelength-controlled beam generator (WCBG1). Focused beams with different orbital angular momentum (OAM) states (l = 0, 1, 2) are generated at red, green, and blue, respectively. (c) Schematic view of the second wavelength-dependent beam generator (WCBG2). Light is focused (l = 0) for red and green light and forms a donut shape for blue light. (d) The phase shifter consists of a titanium dioxide (TiO_2) nanopillar on top of a silver (Ag) substrate with an intermediate thin layer of silicon dioxide (SiO_2). The nanopillars are $H1$ = 600 nm tall and have square cross sections. The reflection phase can be controlled by adjusting the width. The thickness of silicon dioxide and silver layers is $H2$ = 180 nm and $H3$ = 1100 nm, respectively. The TiO_2 nanopillar has a width of W and is patterned with the unit cell size U = 450 nm.

To design a MAM, one needs to engineer the phase profiles at different wavelengths such that their focal lengths coincide. High numerical aperture (NA) high efficiency metalenses with diffraction-limited focusing and subwavelength imaging resolution have been demonstrated in the visible spectrum.[7] However, most of the previously reported metalenses are monochromatic and exhibit a strong chromatic dispersion. This can be beneficial for the design of compact spectrometers,[20,21] but detrimental for a variety of applications ranging from microscopy to photography, wherever different wavelengths are required to be focused at the same distance. MAMs are especially desirable in wearable optical components and displays, where the optical source combines several discrete wavelengths (normally red, green, and blue (RGB) light).

Another example is the wavelength-controlled beam generator (WCBG), which generates beams with different orbital angular momentum (OAM) states at desired wavelengths [Figure 1b,c]. Such device introduces a coupling term between wavelength and OAM states and may lead to novel physical phenomena. One can think of it as essentially a counterpart of spin–orbital angular momentum coupling in the spectral domain. The WCBG can function as a converter between wavelength and OAM multiplexing schemes, allowing information to be directly translated from the spectral domain

to OAM states [Figure 1b], which is difficult to realize in traditional devices, and could find applications in communication. In addition, the WCBG can be designed to realize a compact stimulated emission depletion (STED) microscope. In a STED microscope, an excitation spot and a donut-shaped depletion beam are applied simultaneously to fluorescent samples to achieve super resolution imaging.[35] Conventional STED microscopes handle the excitation, depletion beam, and fluorescent signal separately, which makes the device bulky and adds complexity to the system alignment. A WCBG that focuses light at the excitation and signal wavelengths, and simultaneously generates a focused donut beam at the depletion wavelength [Figure 1c] can integrate the three required functionalities of STED in a single element, thus greatly reduces the device footprint and alignment complexity.

Previous studies on wavelength-controlled metasurfaces have mainly adopted two approaches. The first approach is spatial or spectral multiplexing in which individual phase shifters are optimized for only one wavelength.[36−42] Multiwavelength operation is then achieved by spatially interleaving the phase shifters specifically designed for each wavelength. Usually either in-plane spatial multiplexing (several subpixels)[36−40] or vertical stacking of multiple metasurfaces (several layers)[42] is utilized. Multispectral operation based on the principle of holography and the broad-band property of the berry phase has also been reported.[43] However, these methods have several intrinsic limitations. The interleaving and cross-talk between different structures designed for different wavelengths can degrade image quality and can produce ghost images and unwanted diffraction orders. In addition, spatial multiplexing sets an inherent limit to their maximum efficiency. Vertical stacking requires complicated fabrication techniques. The second approach, dispersion engineering of phase shifters, can potentially break away from these limitations, offering a higher image quality and efficiency. In this method, individual phase shifters are engineered to fulfill simultaneously target phases at all design wavelengths. This approach has been utilized to design MAM in the near-infrared,[44−47] terahertz,[48] and microwave regime,[49−51] but a similar design in the visible spectrum remains challenging. Recently, metalenses with a tailored chromatic response in the visible spectrum were demonstrated.[52,53] However, the methods used in designing broad-band achromatic focusing in general cannot be easily adapted to achieving multifunctionality at discrete wavelengths. In the former case, achromaticity is primarily dominated by the phase and group delay (first-order dispersion) of the phase shifters. To maintain a broad-band performance, the phase shifters need to be designed to exhibit smooth dispersive responses and avoid sharp resonances. This prevents the device from implementing completely distinct tasks at different wavelengths, since the latter usually requires dramatic phase changes, which can not be provided by the lowest (first, second, third, etc.) orders of dispersion. In addition, the device sizes in refs 52 and 53 are limited to tens of micrometers because of the requirement that a large group delay, which scale with the device size, has to be maintained over a large bandwidth. As the group delay is proportional to the Q factor, this goes back to the well-known Q factor–bandwidth limit and presents a fundamental challenge to the previous design methods. However, in our design, we deliberately include sharp resonances to our advantage. These resonances can effectively decouple the realized phases at different wavelengths, allowing independent control of metasurface functions at multiple discrete wavelengths and achieving

significantly larger devices without the complication of the phase shifters' geometry. From a practical point of view, there are many applications that do not require operation over a continuous bandwidth, such as virtual reality display, which only involves achromatic focusing at several discrete wavelengths in the visible spectrum. In those applications, our method can allow more flexibility in the control of device size and multifunctionality.

In this paper, we demonstrated a MAM that has the same focal length for four different wavelengths (460 nm for blue, 540 nm for green, 567 nm for yellow, and 700 nm for red) in the visible spectrum [Figure 1a] and two WCBG designs: WCBG1 generates focused beams with different OAM states (l = 0, 1, and 2) for red, green, and blue light, respectively [Figure 1b]; WCBG2 functions as a focusing lens for green and red light and produces a focused donut beam for blue light [Figure 1c]. An RGB hologram is also simulated to prove the versatility of our design method.

Design Principle. We can denote the target phase profile for a general wavelength-controlled metasurface as

$$\phi(x,y,\lambda_i) = f(x,y,\lambda_i) + C(\lambda_i) \qquad i = 1,2\ldots n \qquad (1)$$

where λ is the design wavelength, (x,y) specifies positions on the metasurface, and n is the number of operating wavelengths. $\phi(x,y,\lambda_i)$ consists of two parts: a general function $f(x,y,\lambda_i)$ that depends on both position and wavelength and a reference phase $C(\lambda_i)$ that is only wavelength dependent. Notably, the functionality at each wavelength is determined only by $f(x,y,\lambda_i)$. This allows us to use $C(\lambda_i)$ as a tuning knob in the design.

To realize a wavelength-dependent target phase profile, the corresponding phase shifter at each position (x,y) needs to simultaneously fulfill the target phases $\phi(x,y,\lambda_i)$ for all design wavelengths $\lambda_1,\lambda_2\ldots\lambda_n$. In many cases, the target phases at two positions can be the same for one wavelength $\phi(x_1,y_1,\lambda_1) = \phi(x_2,y_2,\lambda_1)$, but very different at other wavelengths $\phi(x_1,y_1,\lambda_{j=2\ldots n}) \neq \phi(x_2,y_2,\lambda_{j=2\ldots n})$. This requires having many phase shifters that implement similar phases at λ_1, but different phases at $\lambda_{j=2\ldots n}$. In other words, one needs to build a phase library where the realized phases at different wavelengths are effectively decoupled. In contrast, monochromatic operation needs only one phase shifter for a given realized phase at λ. In the latter, the realized phases at all other wavelengths are predetermined: one loses the degree of freedom to independently implement different phases at different wavelengths [Figure S1].

To effectively decouple the realized phases at different wavelengths, we utilize the folding of phases into $0-2\pi$. The schematic view of our phase shifter is shown in Figure 1d: it consists of a 600 nm tall titanium dioxide (TiO_2) square nanopillar on top of a silver (Ag) mirror, separated by an intermediate silicon dioxide (SiO2) layer. The only geometric parameter that varies across the metasurface is the nanopillar width. The effect of phase folding is revealed by comparing Figure 2a,b. In Figure 2a, each circular point represents a specific nanopillar, with the marker color indicating the pillar width. The Cartesian coordinates correspond to the unfolded realized phase at 460, 540, and 700 nm. Only three wavelengths are considered here for easier visualization. One can see that all of the points form a line. The range of the line is referred to as the phase coverage. Figure 2a is similar to Figure 2b, except that the phases are folded into $0-2\pi$. Now all of the data points form a cloud of points spreading out on the entire $2\pi \times 2\pi \times 2\pi$ cube (phase space), reflecting the decoupling of realized
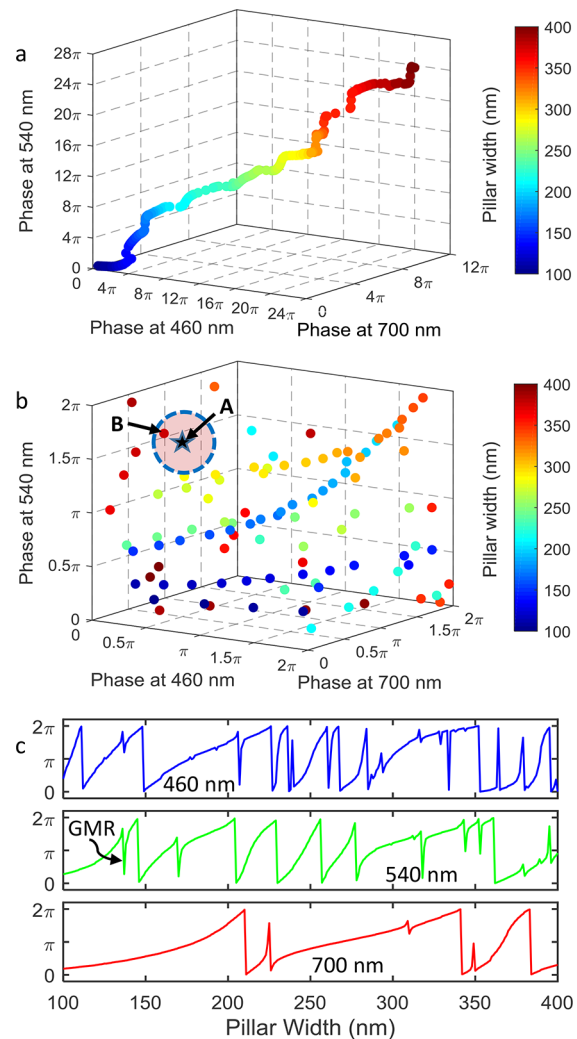

Figure 2. (a) Unfolded realized phases at 460, 540, and 700 nm. Each circular point corresponds to a specific designed nanopillar (phase shifter). Color map represents the pillar width. (b) Realized phases at 460, 540, and 700 nm folded into $0-2\pi$. Each circular point corresponds to a specific designed nanopillar (phase shifter). Color map represents the pillar width. The black star A represents an arbitrary target phase point. Point B is the nearest neighbor of A among all realized phase points. (c) Realized phase as a function of nanopillar width at wavelengths of 460, 540, and 700 nm. As the pillar width changes from 100 to 400 nm, the corresponding phase undergoes multiple $0-2\pi$ phase cycles. The sharp phase jumps reflect the excitation of guided mode resonance (GMR). One example of GMR at a wavelength of 540 nm is marked out explicitly.

phases at different wavelengths. Here the key concept is the folding of phases into $0-2\pi$. The folding process is essentially a nonlinear mapping and breaks the one-on-one relation of the unfolded quantities. Importantly, the unfolded phases have to cover more than 2π, otherwise the folding becomes a trivial identity mapping.

Phase folding provides a possible mechanism of decoupling realized phases, but it still needs a sufficiently large phase coverage to successfully realize a wavelength-controlled metasurface. To understand this, consider the target phase $\phi(x,y,\lambda_{i=1,2,3})$ at a specific position (x,y), represented by a black star A in Figure 2b. We can find its nearest neighbor point (B) in the phase library. The distance between them reflects the phase error of using B to approximate A. Since, in general, the

target phase point A can be located anywhere in the phase space, it is necessary to have a phase library that occupies the entire phase space with a relatively high average local density of points. More phase coverage increases the average local density of points and thus reduces error between realized and target phases. Therefore, achieving a large phase coverage is a crucial step in designing wavelength-controlled metasurfaces. This is also where dispersion engineering of phase shifters comes in.

Two design strategies are utilized to expand the phase coverage. First, we make use of the reflective configuration to effectively double the propagation phase per pillar compared with the transmissive case. Second, we design the nanopillars to support guided mode resonances (GMR). GMR happens when incident light couples to the leaky surface modes and reradiates into free space via a phase-matching element.[54,55] Rapid phase change occurs around the resonances, contributing to a larger phase coverage and further decoupling of realized phases at different wavelengths. Note that the nanopillar center-to-center distance (U) has to be larger than all operation wavelengths in TiO$_2$ to satisfy the required coupling condition. In the meantime, U must be smaller than $\lambda/2NA$ and λ as well to satisfy the Nyquist sampling criterion and avoid higher order diffraction, respectively. Figure 2c shows the realized phases at a function of pillar width at 460, 540, and 700 nm. Notice the relatively sharp phase jumps corresponding to the GMRs.[56] Through both the reflective configuration and GMR, a phase coverage as large as 28π is achieved [Figure 2a].

Method. Earlier, we visualized the error between the target and realized phase as the distance between the nearest neighbor pair in the phase space. However, in practice, one also needs to consider the error in amplitude. In the optimization, we account for both amplitude and phase by comparing the complex field. The average error is defined as the mean Euclidean distance between the target complex field and the realized complex field.

$$\Delta = \frac{1}{N} \sum_{\lambda_i} \sum_{x,y} |t_t \exp(i\phi_t) - t_r \exp(i\phi_r)| \qquad i = 1,2 \dots n \tag{2}$$

where the subscript t and r indicates a target and realized quantity, n is the number of operating wavelengths, and N is a normalization factor. The target amplitude t_t is assumed to be the unity in all of our designs, and the target phase profile ϕ_t is defined in eq 1. The realized amplitude and phase are denoted as t_r and ϕ_r, respectively. The summation is taken over all positions (x,y) on the metasurface and all design wavelengths $\lambda_i(i = 1,2\dots n)$. Particle swarm optimization toolbox (from Matlab) is used to minimize the error function. The reference phase $C(\lambda_i)$ (defined in eq 1) is utilized as an optimization parameter to offer an additional degree of freedom. The Fresnel–Kirchhoff integration method is then used to evaluate the performance of the optimized design.

To design the RGB hologram, we first decompose the target image into its R, G, and B channels. The iterative Fourier transform algorithm (IFTA) is used to obtain the target phase profile at each wavelength. The above-mentioned optimization method is applied to find the optimal choice of phase shifters. We then simulate the reconstructed holographic image using the phase and reflectance of the designed structure via fast Fourier transform.

We first deposited a 1100 nm thick silver (Ag) layer on a silicon substrate using the method described in[57] ref 53. The Ag layer was initially covered with 50 nm thick aluminum oxide (Al$_2$O$_3$) to prevent oxidation during storage. The Al$_2$O$_3$ layer was removed by HF before use. After removing Al$_2$O$_3$, a 180 nm thick silicon dioxide (SiO$_2$) layer was deposited via plasma enhanced chemical vapor deposition (PECVD) on top of Ag. The titanium dioxide (TiO$_2$) nanopillars were then fabricated following the same procedure as mentioned in[58] ref 54. The optical image and scanning electron microscope image of the fabricated samples are shown in Figure 3.
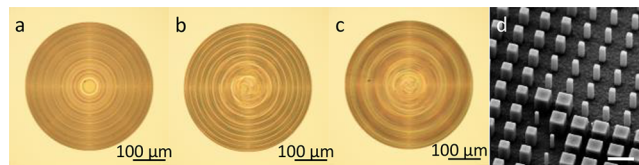

Figure 3. (a−c) Optical image of the fabricated (a) multiwavelength achromatic metalens (MAM), (b) wavelength-controlled beam generator 1 (WCBG1), (c) wavelength-controlled beam generator 2 (WCBG2). (d) SEM image of a section of the fabricated WCBG1. Scale bar: 500 nm.

A custom-built setup [Figure S2] is used to characterize the fabricated samples. A laser beam from a supercontinuum laser (NKT Photonics) is collimated and used to illuminate the metasurface at normal incidence. We inserted a 50:50 beam splitter between the source and the samples to direct the reflected light to the imaging system. Two sets of objectives with their tube lenses are cascaded to achieve a magnification of 40. The magnification factor is verified by imaging a target of known size. A high dynamic range cMOS camera is used to capture images. The sample is mounted on a motorized stage with a minimum movement step of 100 nm. During the measurement, the sample is moved along the z-axis (propagation direction) and the images are captured accordingly. In the first measurement of MAM, the stage is moved in steps of 10 μm from 0.18 to 1.78 mm to capture a larger z range. In the second measurement of MAM, the step size is set to 3 μm to characterize the beam propagation near the focal spot ($z = 0.901−1.057$ mm). The measurement is automated with the help of a user-customized Labview program that controls the laser, motorized stage, and camera simultaneously.

To measure the focused power, we placed an iris with an adjustable diameter (D) in the image plane. The iris diameter is set to 0.25 mm to block out the zeroth-order light and allow the first ring of the Airy disk focal spot passing through. A power meter is placed immediately after the iris to collect the focused light. To measure the reference power, the MAM is replaced by a silver mirror of the same size ($D = 400$ μm), and the iris is opened. Since the image of the mirror after the second objective is larger than the receivable area ($D = 9$ mm) of the power meter, we measure its power after the first objective and then adjusted the value according to the transmittance through the second objective. We first use a silver mirror with smaller size ($D = 200$ μm) such that its image after the second objective can be fully captured by the power meter. The reflected power after the first and second objective is recorded, respectively. Their ratio is then used to adjust the reflected power from the $D = 400$ μm silver mirror. Focusing efficiency is calculated as the ratio of the focused power and the adjusted reference power.
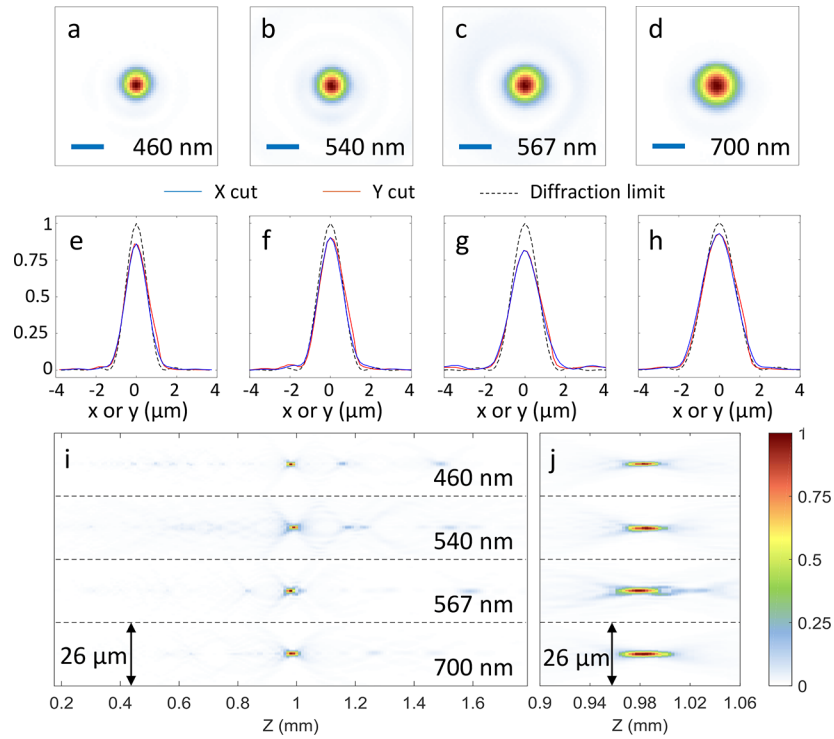
Figure 4. (a−d) Focal spot images of the multiwavelength achromatic metasurface (MAM) at (a) 460, (b) 540, (c) 567, and (d) 700 nm. The corresponding focal length is 0.979, 0.985, 0.976, 0.982 mm, respectively. Scale bar: 2 μm. (e−h) Blue/red curve: measured intensity profile along the horizontal (x)/vertical (y) line cutting through the center of the focal spot at (e) 460 nm, (f) 540 nm, (g) 567 nm, and (h) 700 nm. Black dashed curve: intensity profile of the diffraction-limited focal spot with the unity peak intensity. The measured profiles are normalized to yield the same focused power as the theoretical ones. (i) Measured intensity profiles of the reflected beam by MAM in the x−z plane at the wavelength of 460, 540, 567, and 700 nm from z = 0.18−1.78 mm. (j) Magnified measured intensity profile in the x−z plane from z = 0.901−1.057 mm.

Results. As a first example of wavelength-controlled metasurface, we designed a MAM with NA = 0.2 and D = 400 μm. The target phase profile is given by

$$\phi(r,\lambda_i) = \frac{2\pi}{\lambda_i}\left(f - \sqrt{r^2 + f^2}\right) + C(\lambda_i) \tag{3}$$

where f is the focal length. The lens exhibits achromatic focusing at wavelengths of 460 (B), 540 (G), 567 (Y), and 700 nm (R). The measured focal spot images are shown in Figure 4a−d. Focal length was measured as 0.979, 0.985, 0.976, and 0.982 mm at the B, G, Y, and R wavelength, respectively [Figures 4i,j]. Near-diffraction-limited focal spots are achieved with Strehl ratios of 0.86, 0.91, 0.81, and 0.92 at corresponding wavelengths [Figure 4e−h]. The measured focusing efficiencies are 17.7%, 16.0%, 21.4%, and 22.6% for B, G, Y, and R, respectively. Figure 4i shows the evolution of the reflected beam in the x−z plane from z = 0.18−1.78 mm. The measured intensity profile is in good agreement with simulation [Figure S3]. Residual unwanted higher order focal spots are observed, but with intensity much lower than the primary focal spots. A zoom-in view of the x−z plane propagation profile near the focal plane is illustrated in Figure 4j. It is clear that B, G, Y, and R light all focuses at nearly the same position. A comparison between the target and realized phase profile is shown in Figures S4 and S5.

We also designed metasurfaces that generate focused beams with a different OAM depending on wavelength (wavelength-controlled beam generator, WCBG).

The target phase profile for WCBG is given by

$$\phi(r,\theta,\lambda_i,l_i) = \frac{2\pi}{\lambda_i}\left(f - \sqrt{r^2 + f^2}\right) + l_i\theta + C(\lambda_i) \tag{4}$$

where (r,θ) is the cylindrical coordinates on the metasurface, l_i is the OAM quantum number at λ_i, and f is the focal length. The phase profile contains an achromatic focusing term $\frac{2\pi}{\lambda_i}\left(f - \sqrt{r^2 + f^2}\right)$, a helical phase term $l_i\theta$, and a reference phase $C(\lambda_i)$. Here, we design the metalenses with NA = 0.2, f = 0.98 mm, and diameter of 400 μm.

If $l = 0$, then eq 4 reduces to eq 3 and the device functions as a normal focusing lens. For $l \neq 0$, the device generates a donut-shaped focal spot. The achromatic focusing term (first term on the right side of eq 4) can be generalized to have a wavelength-dependent focal distance or removed if desired. Note that a rigorous treatment of the focused optical vortex beam involves the vector diffraction theory. The latter requires considering both polarization effect and spin−orbital angular momentum conversion, especially in the case of the tightly focused vortex beam.[59] However, our design (NA = 0.2) is far from the strongly focused beam regime, and one can safely use the scalar diffraction theory.

Two examples of WCBG are fabricated. Figure 5 shows the measured intensity profile of one device (WCBG1) that generates a focused beam with l = 2, 1, 0 at wavelength 455, 540, and 700 nm, respectively, with a corresponding efficiency of 31%, 37%, and 33%. The average efficiency is 34%, comparable to the theoretical upper limit of average efficiency using spatial multiplexing (33.4%). The experimental results agree well with numerical simulations [Figures 5d−f].
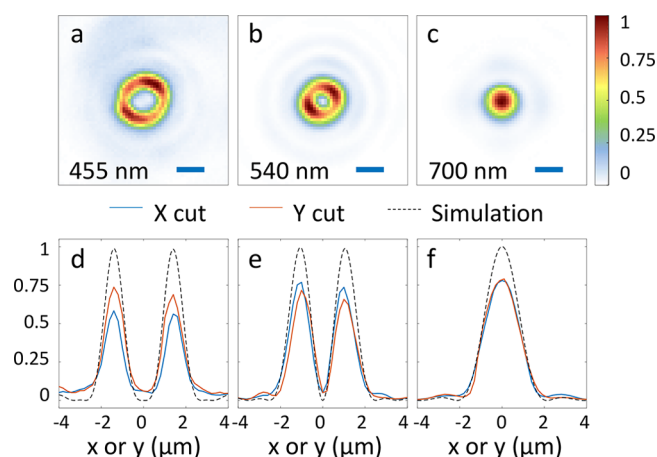
Figure 5. (a−c) Measured intensity profile of wavelength-controlled beam generator 1 (WCBG1) at $z = 0.98$ mm. The device generates (a) a large focused donut beam ($l = 2$) at 455 nm, (b) a small focused donut beam ($l = 1$) at 540 nm, and (c) a focal spot ($l = 0$) at 700 nm at the same focal plane. Scale bar: 2 μm. (d−f) Blue/red curve: measured intensity profile along the horizontal (x)/vertical (y) line cutting through the center of the beam in the focal plane. Black dashed curve: simulated intensity profile with the unity peak intensity. The measured profiles are normalized to yield the same focused power as the simulated ones.

The measurement results of a different design (WCBG2) that generates a focused beam with $l = 1, 0, 0$ at 480, 515, and 690 nm, respectively, at $z = 0.98$ mm are illustrated in Figure 6.
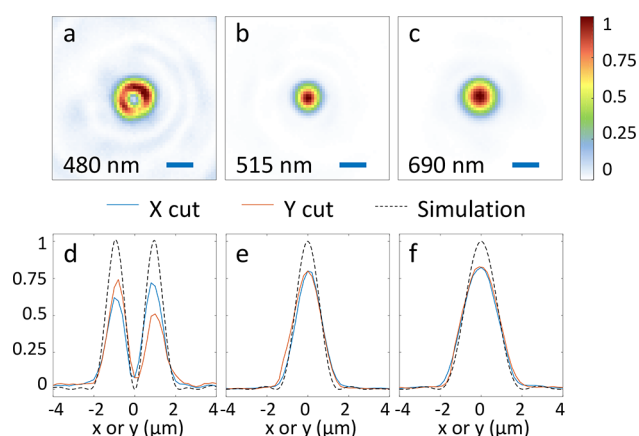

Figure 6. (a−c) Measured intensity profile of wavelength-controlled beam generator 2 (WCBG2) at $z = 0.98$ mm. The device generates (a) a focused donut beam ($l = 1$) at 480 nm, a focal spot ($l = 0$) at (b) 515 nm, and (c) 690 nm at the same focal plane. Scale bar: 2 μm. (d−f) Blue/red curve: measured intensity profile along the horizontal (x)/vertical (y) line cutting through the center of the beam in the focal plane. Black dashed curve: simulated intensity profile with the unity peak intensity. The measured profiles are normalized to yield the same focused power as the simulated ones.

The efficiency is 31%, 32%, and 33% at each operating wavelength. With the ability to focus light at two wavelengths, and generate a focused donut-shaped beam at a third wavelength, WCBG2 serves as a proof-of-principle prototype for a compact STED microscope. Note, however, that a true STED microscope requires a high NA, and therefore the polarization effect becomes non-negligible. In that case, the design principle remains similar, but a proper incident

polarization and vector diffraction theory need to be considered. Simulation results of a high NA design (NA = 0.8) can be found in the supplementary file (Figure S8a−c). The donut beams profiles [Figures 5a,b and 6a] show a slight asymmetry in both devices due to imperfect phase fitting and optical alignment.

To demonstrate the versatility of our design approach, we also simulated a full color hologram (Figure 7) operating at 480, 530, and 630 nm. The target image was well-reconstructed, although the contrast is reduced due to phase fitting error.
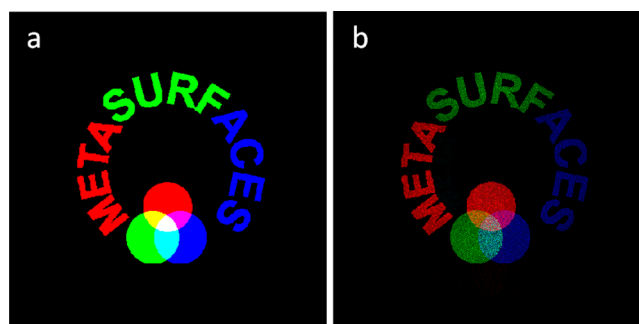

Figure 7. (a) Target image and (b) the simulated holographic image of a RGB hologram designed at 480, 530, and 630 nm.

Although we emphasize the importance of having multiple 2π phase coverages, our devices should not be confused with multiorder diffractive (MOD) optical elements.[60,61] MOD lenses are diffractive lenses operating at higher diffraction orders. Unlike traditional diffractive lenses, the phase jump of MOD lenses at the zone boundaries is a multiple of 2π to allow for higher diffraction orders. With proper engineering, the mth-order focal spot at λ_1 can coincide with the nth-order focal spot at λ_2 ($\lambda_1 > \lambda_2, m < n$). By tuning the blazing angle, MOD lenses can achromatically focus light at several wavelengths with high efficiency. Although the term multiple 2π phase is used in both cases, there are major differences between our method and MOD designs. First, MOD cannot implement different functionalities at different wavelengths. In comparison, in our design, the functionality at different wavelengths can be completely decoupled. Second, MOD devices trade achromatism with thickness. The thickness of visible MOD lenses, in general, increases with the number of wavelengths corrected, whereas our design does not require adding physical thickness or fabrication complexity. In addition, the surface configuration of MOD lenses has a zone period that is a common multiple of the period required at different design wavelengths. This multiplied zone period is the most important feature and a necessary condition for MOD lenses. In contrast, our design has an aperiodic surface configuration, and the achromatic performance is encoded locally in the dispersion property of individual phase shifters.

It is also feasible to adapt the proposed design principle to transmissive configurations. First of all, we believe the basic principles are still applicable. For example, one can use phase folding to decouple the realized phases at different wavelengths and expand the phase coverage as much as possible to reduce error. Second, the essence of the phase shifter design, increasing propagation phase per pillar and incorporating resonances, remains valid, although the actual implementation may vary. More specifically, rather than doubling the propagation phase via reflection, one may increase the pillar height instead;

moreover, other resonance mechanisms can be utilized instead of GMR to achieve a more uniform transmission spectrum.

Strictly speaking, GMR is a collective phenomenon and assumes a periodic boundary condition. On metasurfaces, the nanopillar width varies across the surface and the system is no longer periodic. However, we believe the concept of GMR remains as a good approximation in our system. The high index contrast between nanopillars and air leads to strong coupling between the surface modes and free space radiation. The guided waves are scattered out to free space rapidly and do not propagate far in the lateral direction. This means the modes are essentially localized, with the reflection property depending only on the local geometry around each nanopillar.[62] The agreement between our measured intensity profiles and those simulated via Fresnel−Kirchhoff integration serves as additional proof of the validity of such approximation.

A higher efficiency is expected with further improvement in fabrication. To understand what limits the final efficiency in the current setup, we measured the power of light reflected from the surface of MAM and a silver mirror of the same size. We found that the former is less than 30% of the latter, which suggests that the reflection loss is a main limiting factor to the total efficiency. The ratio of the focused power and the total power reflected from the MAM surface is more than 70% for all wavelengths, indicating a good focusing performance. The reflection loss can result from resonant effect, which causes more energy being absorbed by the metallic mirror. Therefore, by replacing the metallic mirror with a dielectric Distributed Bragg Reflector (DBR), one can potentially increase the efficiency to around 70%.

In summary, we presented a versatile wavelength-controlled metasurface design strategy in the visible spectrum. As a proof-of-principle, we theoretically and experimentally demonstrated a visible multiwavelength achromatic metalens (MAM) operating at B, G, Y, and R wavelengths. We also designed and fabricated two wavelength-controlled beam generators (WCBG) that produce focused beams with different OAM numbers depending on wavelength. A full color hologram is also demonstrated in simulation. The efficiency can be further enhanced through improvement in design and fabrication. The number of operating wavelengths can also be expanded to accommodate a more complex functionality integration.

■ ASSOCIATED CONTENT

Ⓢ Supporting Information
The Supporting Information is available free of charge on the ACS Publications website at DOI: 10.1021/acs.nano-lett.7b05458.

> Phase library of a metasurface operating at 460 nm, measurement setup used for wavelength-controlled metasurfaces characterization, simulated intensity profiles, histograms, comparison of the realized phase and target phase, realized phase and reflectivity for varying pillar width over the visible spectrum, measured focal length of the multiwavelength achromatic metalens, and simulated intensity profiles (PDF)

■ AUTHOR INFORMATION

Corresponding Author
*E-mail: capasso@seas.harvard.edu.

ORCID Ⓘ
Zhujun Shi: 0000-0003-0121-2083

Mohammadreza Khorasaninejad: 0000-0002-0293-9113
Wei Ting Chen: 0000-0001-8665-9241
Michele Tamagnone: 0000-0002-9812-2449
Kundan Chaudhary: 0000-0003-4253-0942

Present Address
(C.R.C.) Department of Electrical Engineering and Computer Science, Massachusetts Institute of Technology, Cambridge, Massachusetts 02139, USA

Author Contributions
○Z.S., M.K., and Y.W.H. contributed equally to this work.

Notes
The authors declare no competing financial interest.

■ REFERENCES

(1) Arbabi, A.; Horie, Y.; Bagheri, M.; Faraon, A. *Nat. Nanotechnol.* **2015**, *10* (11), 937−943.
(2) Lin, D. M.; Fan, P. Y.; Hasman, E.; Brongersma, M. L. *Science* **2014**, *345* (6194), 298−302.
(3) Yu, N.; Capasso, F. *Nat. Mater.* **2014**, *13* (2), 139−150.
(4) Kildishev, A. V.; Boltasseva, A.; Shalaev, V. M. *Science* **2013**, *339* (6125), 1232009.
(5) Yu, N.; Genevet, P.; Kats, M. A.; Aieta, F.; Tetienne, J.-P.; Capasso, F.; Gaburro, Z. *Science* **2011**, *334* (6054), 333.
(6) Paniagua-Dominguez, R.; Yu, Y. F.; Miroshnichenko, A. E.; Krivitsky, L. A.; Fu, Y. H.; Valuckas, V.; Gonzaga, L.; Toh, Y. T.; Kay, A. Y.; Luk'yanchuk, B.; Kuznetsov, A. I. *Nat. Commun.* **2016**, *7*, 10362.
(7) Khorasaninejad, M.; Chen, W. T.; Devlin, R. C.; Oh, J.; Zhu, A. Y.; Capasso, F. *Science* **2016**, *352* (6290), 1190−1194.
(8) Arbabi, A.; Horie, Y.; Ball, A. J.; Bagheri, M.; Faraon, A. *Nat. Commun.* **2015**, *6*, 7069.
(9) Chen, W. T.; Zhu, A. Y.; Khorasaninejad, M.; Shi, Z. J.; Sanjeev, V.; Capasso, F. *Nano Lett.* **2017**, *17* (5), 3188−3194.
(10) Li, X.; Xiao, S.; Cai, B.; He, Q.; Cui, T. J.; Zhou, L. *Opt. Lett.* **2012**, *37* (23), 4940−4942.
(11) Huang, Y. W.; Chen, W. T.; Tsai, W. Y.; Wu, P. C.; Wang, C. M.; Sun, G.; Tsai, D. P. *Nano Lett.* **2015**, *15* (5), 3122−3127.
(12) Ni, X. J.; Kildishev, A. V.; Shalaev, V. M. *Nat. Commun.* **2013**, *4*, 2807.
(13) Zheng, G. X.; Muhlenbernd, H.; Kenney, M.; Li, G. X.; Zentgraf, T.; Zhang, S. *Nat. Nanotechnol.* **2015**, *10* (4), 308−312.
(14) Devlin, R. C.; Ambrosio, A.; Wintz, D.; Oscurato, S. L.; Zhu, A. Y.; Khorasaninejad, M.; Oh, J.; Maddalena, P.; Capasso, F. *Opt. Express* **2017**, *25* (1), 377−393.
(15) Jin, J.; Luo, J.; Zhang, X.; Gao, H.; Li, X.; Pu, M.; Gao, P.; Zhao, Z.; Luo, X. *Sci. Rep.* **2016**, *6*, 24286.
(16) Mehmood, M. Q.; Mei, S. T.; Hussain, S.; Huang, K.; Siew, S. Y.; Zhang, L.; Zhang, T. H.; Ling, X. H.; Liu, H.; Teng, J. H.; Danner, A.; Zhang, S.; Qiu, C. W. *Adv. Mater.* **2016**, *28* (13), 2533−2539.

(17) Shalaev, M. I.; Sun, J.; Tsukernik, A.; Pandey, A.; Nikolskiy, K.; Litchinitser, N. M. *Nano Lett.* **2015**, *15* (9), 6261−6266.

(18) Chen, W. T.; Khorasaninejad, M.; Zhu, A. Y.; Oh, J.; Devlin, R. C.; Zaidi, A.; Capasso, F. *Light: Sci. Appl.* **2016**, *6*, e16259.

(19) Pu, M. B.; Li, X.; Ma, X. L.; Wang, Y. Q.; Zhao, Z. Y.; Wang, C. T.; Hu, C. G.; Gao, P.; Huang, C.; Ren, H. R.; Li, X. P.; Qin, F.; Yang, J.; Gu, M.; Hong, M. H.; Luo, X. G. *Sci. Adv.* **2015**, *1* (9), e1500396.

(20) Khorasaninejad, M.; Chen, W. T.; Oh, J.; Capasso, F. *Nano Lett.* **2016**, *16* (6), 3732−3737.

(21) Zhu, A. Y.; Chen, W. T.; Khorasaninejad, M.; Oh, J.; Zaidi, A.; Mishra, I.; Devlin, R. C.; Capasso, F. *Apl Photonics* **2017**, *2* (3), 036103.

(22) Chen, W. T.; Torok, P.; Foreman, M. R.; Liao, C. Y.; Tsai, W. Y.; Wu, P. R.; Tsai, D. P. *Nanotechnology* **2016**, *27* (22), 224002.

(23) Mueller, J. P. B.; Leosson, K.; Capasso, F. *Optica* **2016**, *3* (1), 42−47.

(24) Wei, S. W.; Yang, Z. Y.; Zhao, M. *Opt. Lett.* **2017**, *42* (8), 1580−1583.

(25) Cheng, H.; Wei, X.; Yu, P.; Li, Z.; Liu, Z.; Li, J.; Chen, S.; Tian, J. *Appl. Phys. Lett.* **2017**, *110* (17), 171903.

(26) Cai, T.; Tang, S.; Wang, G.; Xu, H.; Sun, S.; He, Q.; Zhou, L. *Adv. Opt. Mater.* **2017**, *5* (2), 1600506.

(27) Maguid, E.; Yulevich, I.; Yannai, M.; Kleiner, V.; L Brongersma, M.; Hasman, E. *Light: Sci. Appl.* **2017**, *6* (8), e17027.

(28) Wen, D.; Yue, F.; Ardron, M.; Chen, X. *Sci. Rep.* **2016**, *6*, 27628.

(29) Wen, D.; Chen, S.; Yue, F.; Chan, K.; Chen, M.; Ardron, M.; Li, K. F.; Wong, P. W. H.; Cheah, K. W.; Pun, E. Y. B.; Li, G.; Zhang, S.; Chen, X. *Adv. Opt. Mater.* **2016**, *4* (2), 321−327.

(30) Eisenbach, O.; Avayu, O.; Ditcovski, R.; Ellenbogen, T. *Opt. Express* **2015**, *23* (4), 3928−36.

(31) Maguid, E.; Yulevich, I.; Veksler, D.; Kleiner, V.; Brongersma, M. L.; Hasman, E. *Science* **2016**, *352* (6290), 1202−1206.

(32) Xiao, S.; Wang, J.; Liu, F.; Zhang, S.; Yin, X.; Li, J. *Nanophotonics* **2017**, *6* (1), 215−234.

(33) Xu, H.-X.; Tang, S.; Ling, X.; Luo, W.; Zhou, L. *Ann. Phys.* **2017**, *529* (5), 1700045.

(34) Balthasar Mueller, J. P.; Rubin, N. A.; Devlin, R. C.; Groever, B.; Capasso, F. *Phys. Rev. Lett.* **2017**, *118* (11), 113901.

(35) Hell, S. W.; Wichmann, J. *Opt. Lett.* **1994**, *19* (11), 780−782.

(36) Li, K.; Guo, Y.; Pu, M.; Li, X.; Ma, X.; Zhao, Z.; Luo, X. *Opt. Express* **2017**, *25* (18), 21419.

(37) Zhao, W. Y.; Liu, B. Y.; Jiang, H.; Song, J.; Pei, Y. B.; Jiang, Y. Y. *Opt. Lett.* **2016**, *41* (1), 147−150.

(38) Arbabi, E.; Arbabi, A.; Kamali, S. M.; Horie, Y.; Faraon, A. *Sci. Rep.* **2016**, *6*, 32803.

(39) Wang, B.; Dong, F.; Li, Q. T.; Yang, D.; Sun, C.; Chen, J.; Song, Z.; Xu, L.; Chu, W.; Xiao, Y. F.; Gong, Q.; Li, Y. *Nano Lett.* **2016**, *16* (8), 5235−5240.

(40) Yang, K.; Pu, M.; Li, X.; Ma, X.; Luo, J.; Gao, H.; Luo, X. *Nanoscale* **2016**, *8* (24), 12267−71.

(41) Fan, Q. B.; Huo, P. C.; Wang, D. P.; Liang, Y. Z.; Yan, F.; Xu, T. *Sci. Rep.* **2017**, *7*, 45044.

(42) Avayu, O.; Almeida, E.; Prior, Y.; Ellenbogen, T. *Nat. Commun.* **2017**, *8*, 14992.

(43) Arbabi, E.; Arbabi, A.; Kamali, S. M.; Horie, Y.; Faraon, A. *Optica* **2016**, *3* (6), 628.

(44) Khorasaninejad, M.; Aieta, F.; Kanhaiya, P.; Kats, M. A.; Genevet, P.; Rousso, D.; Capasso, F. *Nano Lett.* **2015**, *15* (8), 5358−5362.

(45) Zhao, Z. Y.; Pu, M. B.; Gao, H.; Jin, J. J.; Li, X.; Ma, X. L.; Wang, Y. Q.; Gao, P.; Luo, X. G. *Sci. Rep.* **2015**, *5*, 5.

(46) Arbabi, E.; Arbabi, A.; Kamali, S. M.; Horie, Y.; Faraon, A. *Optica* **2017**, *4* (6), 625.

(47) Aieta, F.; Kats, M. A.; Genevet, P.; Capasso, F. *Science* **2015**, *347* (6228), 1342−1345.

(48) Qu, S.-W.; Wu, W.-W.; Chen, B.-J.; Yi, H.; Bai, X.; Ng, K. B.; Chan, C. H. *Sci. Rep.* **2015**, *5*, 9367.

(49) Peng, J. J.; Qu, S. W. Ultra-wideband reflectarray with multi-resonance elements. *Applied Computational Electromagnetics Society Symposium (ACES)* **2017**, 1−2.

(50) Capozzoli, A.; Curcio, C.; Liseno, A.; Migliorelli, M.; Toso, G. Phase-only synthesis of conformal aperiodic reflectarrays with multi-frequency specifications. *Antennas and Propagation (EUCAP), 2012 6th European Conference on* **2012**, 2220−2224.

(51) Mayumi, K.; Deguchi, H.; Tsuji, M. Wideband single-layer microstrip reflectarray based on multiple-resonance behavior. *2008 IEEE Antennas and Propagation Society International Symposium,* **2008**, 1−4.

(52) Chen, W. T.; Zhu, A. Y.; Sanjeev, V.; Khorasaninejad, M.; Shi, Z.; Lee, E.; Capasso, F. *Nat. Nanotechnol.* **2018**, 1.

(53) Wang, S.; Wu, P. C.; Su, V. C.; Lai, Y. C.; Chen, M. K.; Kuo, H. Y.; Chen, B. H.; Chen, Y. H.; Huang, T. T.; Wang, J. H.; Lin, R. M.; Kuan, C. H.; Li, T.; Wang, Z.; Zhu, S.; Tsai, D. P. *Nat. Nanotechnol.* **2018**, 1.

(54) Wang, S. S.; Magnusson, R. *Appl. Opt.* **1993**, *32* (14), 2606−2613.

(55) Fan, S. H.; Joannopoulos, J. D. *Phys. Rev. B: Condens. Matter Mater. Phys.* **2002**, *65* (23), 235112.

(56) Khorasaninejad, M.; Shi, Z.; Zhu, A. Y.; Chen, W. T.; Sanjeev, V.; Zaidi, A.; Capasso, F. Achromatic metalens over 60 nm bandwidth in the visible and metalens with reverse chromatic dispersion. *Nano Lett.* **2017**, *17* (3), 1819−1824.

(57) High, A. A.; Devlin, R. C.; Dibos, A.; Polking, M.; Wild, D. S.; Perczel, J.; de Leon, N. P.; Lukin, M. D.; Park, H. *Nature* **2015**, *522* (7555), 192−196.

(58) Devlin, R. C.; Khorasaninejad, M.; Chen, W. T.; Oh, J.; Capasso, F. *Proc. Natl. Acad. Sci. U. S. A.* **2016**, *113* (38), 10473−10478.

(59) Zhao, Y. Q.; Edgar, J. S.; Jeffries, G. D. M.; McGloin, D.; Chiu, D. T. *Phys. Rev. Lett.* **2007**, *99* (7), 073901.

(60) Sweeney, D. W.; Sommargren, G. E. *Appl. Opt.* **1995**, *34* (14), 2469−2475.

(61) Faklis, D.; Morris, G. M. *Appl. Opt.* **1995**, *34* (14), 2462−2468.

(62) Fattal, D.; Li, J. J.; Peng, Z.; Fiorentino, M.; Beausoleil, R. G. *Nat. Photonics* **2010**, *4* (7), 466−470.